3D-ZIF scaffold derived carbon encapsulated iron nitride as a synergistic catalyst for ORR and zinc-air battery cathodes

Amr Radwan [a, b, c], Huihui Jin [b, c], Bingshuai Liu [c], Zibo Chen [c], Qian Wu [c], Xin Zhao [a], Daping He [a, c, **], Shichun Mu [b, c, *]

[a] School of Science, Wuhan University of Technology, Wuhan, 430070, China
[b] Foshan Xianhu Laboratory of the Advanced Energy Science and Technology Guangdong Laboratory, Xianhu Hydrogen Valley, Foshan, 528200, China
[c] State Key Laboratory of Advanced Technology for Materials Synthesis and Processing, Wuhan University of Technology, Wuhan, 430070, China

ARTICLE INFO

ABSTRACT

To commercialize fuel cells and metal-air batteries, it is intensely desirable but challenging to design highly active, earth-abundant, low-cost and stable oxygen reduction reaction (ORR) catalysts to replace rare, precious and unstable Pt-based ones. Among them, Fe_3N is one of the promising candidates to replace precious and unstable Pt-based ORR catalysis. Herein, to obtain Fe_3N nanoparticles encapsulated in carbon frameworks with rich doped nitrogen, Fe_2O_3 nanoparticles are firstly prepared hydrothermally and converted to Fe_3N, and then 3D zeolitic-imidazole frameworks (ZIF) is applied as a scaffold unit, followed by pyrolysis under ammonia gas. The product annealed at 900 °C (ZFN-900) displays a higher half-wave potential (25 mV) than a carbon-supported Pt catalyst in alkaline media. Remarkably, as air electrodes of the zinc-air battery, it exhibits a raised power density peak at 115.8 mW cm^{-2} with respect to carbon-supported Pt (81.6 mW cm^{-2}) in addition to outstanding durability. Such superior catalytic properties are broadly accredited to the chemical structure synergistic effect, extraordinary surface area, rich active sites, conductive carbon frameworks with highly nitrogen doping. Without a doubt, this method sets out a novel pathway for advantageous and extremely active catalysts with an adapted design for electrochemical energy systems.

© 2020 Elsevier Ltd. All rights reserved.

1. Introduction

Recently, the expanding adverse outcomes of out-of-date fuels on energy and atmosphere are promoting intensive attempts to expand the technologies of green renewable energy, incorporating fuel cells [1,2], secondary batteries [3—5] and other energy conversion systems [6,7]. The oxygen reduction reaction (ORR) is amongst the vigorous cores of the electrochemical processes in fuel cells and metal-air batteries. In consequence of the high catalytic activity, noble metal catalysts such as carbon-supported platinum (Pt/C) materials have been recognized as extremely efficient for ORR. Nevertheless, the increasing price and inferior stability of such catalysts have prohibited the technologies of green renewable energy towards fuel cells and zinc-air batteries from broad-scale applications. Consequently, it is extremely desirable to use alternative ORR catalysts on the bases of a transition metal, with high catalytic activity, high durability in addition to low cost to achieve full large-scale implementation.

Low-cost metal catalysts, in particular metal oxides [8], nitrogen-doped carbon composed with transition metals systems [9], and metal nitrides [10—13], have been possible alternatives to substitute Pt-based catalysts because of their favorable ORR catalytic activities, economical and eco-friendly properties. Among metal nitrides, Fe_3N-based catalysts [10,14] display excellent ORR catalytic activity, even analogous to the commercial Pt/C. However, like other nanomaterials [11], Fe_3N nanoparticles have a tendency to agglomerate during the reaction, thus significantly decreasing their activity and stability. Presently, numerous studies are seeking to boost the performance of Fe_3N by means of high porosity materials for instance graphite [10], carbon nanotubes or graphene [15] to diminish agglomeration. However, up till now, the introduced methods for boosting Fe_3N from agglomerations often show subordinate ORR activity, which leads to a sluggish charging efficiency in rechargeable zinc-air batteries, preventing their practical applications. To overcome this obstacle, besides selecting porous

* Corresponding author. Postal address: State Key Laboratory of Advanced Technology for Materials Synthesis and Processing, Wuhan University of Technology, Wuhan, 430070, China.
** Corresponding author. School of Science, Wuhan University of Technology, Wuhan, 430070, China,
E-mail addresses: hedaping@whut.edu.cn (D. He), msc@whut.edu.cn (S. Mu).

materials as support of Fe₃N, the additional advantageous properties of support such as ultra-high Brunauer–Emmett–Teller (BET) surface area, exceptional double-layer capacity (Cdl), extraordinary electrochemical active surface area (ECSA), extremely low charge transfer resistance (R_{ct}), also should be considered. Hence, efficient strategies that enhancing the Fe₃N ORR catalytic performance throughout optimizing the aforementioned properties are urgently needed.

As an important precursor of non-precious metal catalysts, zeolitic-imidazole frameworks (ZIFs) have attracted many researchers' attention, due to their structural flexibility, versatile surface geometry, porosity, N-species and ultra-high surface area [1,16,17]. Through pyrolysis, ZIFs can be post-synthetically transformed to amorphous otherwise graphitic carbon frameworks [18,19], providing an affluent platform of functionally tailored materials for electrocatalytic implementations [20], rechargeable batteries [21] and supercapacitors [22,23]. In addition, the straightforward thermal treatment of ZIFs including metal precursors might produce immense graphitic metal/N-doped nano carbonaceous frameworks [16,24]. Higher graphitization, however, predominantly causes a reduction in doped-N content and porousness [24,25], hindering the charged species diffusion and ORR catalytic activity. Nevertheless, the vast majority of these electrocatalytic materials still have inadequate ORR activity, and therefore unable to meet any actual feasible applications [24].
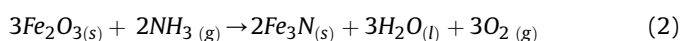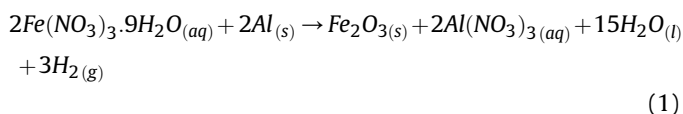
In accordance with this situation, it is extremely advantageous to come up with a new strategy to exaggerate the active size and the surface area. Metal species can be integrated into ZIF holes, thus diminishing their agglomeration, and boosting the catalytic activity and stability of the final materials. Herein, by this new strategy, the structure of Fe₃N embedded in 3D high surface area ZIFs as a precursor could produce nitrogen-doped carbon network encapsulated Fe₃N, and then utilized as an extraordinary cost-effective catalyst for ORR and Zinc-air batteries. This interesting work opens the way for broader applications to design and produce cheaper and more robust electrocatalysts.

2. Experimental section

2.1. Electrocatalyst preparation

2.1.1. Synthesis of Fe₃N nanoparticles

Fe₂O₃ nanoparticles were first prepared and applied as a precursor for Fe₃N production as mentioned in equation (1). Aluminum foil (0.49 g) was immersed in 70 ml of de-ionized water containing Fe(NO₃)₃.9H₂O (21 g) in the autoclave Teflon container. After that, the autoclave was closed and put in the oven at 180 °C for 3 h. The autoclave remained to cool at ambient temperature, then the outcome precipitate of Fe₂O₃ nanoparticles was then gathered by centrifuging and washed many times by de-ionized water. The obtained Fe₂O₃ nanoparticles were left to dry at 60 °C overnight. According to the proposed equation (2), to convert Fe₂O₃ into Fe₃N, a tube oven was used with argon gas to reach 900 °C for 1 h, then cooled to room temperature gradually with argon gas. The obtained black powder was Fe₃N.

$$2Fe(NO_3)_3.9H_2O_{(aq)} + 2Al_{(s)} \rightarrow Fe_2O_{3(s)} + 2Al(NO_3)_{3(aq)} + 15H_2O_{(l)} + 3H_{2(g)}$$

$$\tag{1}$$

$$3Fe_2O_{3(s)} + 2NH_{3(g)} \rightarrow 2Fe_3N_{(s)} + 3H_2O_{(l)} + 3O_{2(g)} \tag{2}$$

2.1.2. Synthesis of Fe₃N encapsulated in ZIF-8

To obtain Fe₃N encapsulated in ZIF-8 (ZFN), Fe₃N nanoparticles (0.15 g) were sonicated in 36 ml methanol containing Zn(NO₃)₂.6H₂O (1.2 g) for 1 h. Afterward, 2-methylimidazole (2.6 g) was dissolved in the sonicated mixture by stirring at 35 °C for 4 h, after that the ZFN was left to dry under vacuum at 60 °C overnight.

2.1.3. Synthesis of ZFN-800, ZFN-900 and ZFN-1000

To achieve Fe₃N encapsulated in N-doped carbon hollow 3D structure at different temperatures, ZFN samples were thermally processed at 800 °C, 900 °C and 1000 °C in the presence of ammonia gas for 1 h, thereby leading to the samples denoted as ZFN-800, ZFN-900 and ZFN-1000, respectively. Moreover, N/C was obtained by annealing ZIF-8 only at 900 °C. To determine the Fe₃N content of the composite, thermogravimetric analysis (TGA) was performed (Fig. S4).

2.2. Materials characterization

Morphologies of the surface were detected on field emission scanning electron microscope (FESEM) (SEM, Zeiss Ultra Plus) and operated at 20 kV. The transmission electron microscope (TEM) and high-resolution TEM (HRTEM) (TEM, HITACHI-8100) observations were performed at 20 kV. Rigaku X-ray diffractometer was used in testing X-ray diffraction (XRD) patterns, at a wavelength of 1.5406 Å through Cu-Kα radiation. Throughout an excitation wavelength of 633 nm, Ar ion laser, Raman shifts were obtained by utilizing LabRAM Aramis Raman spectrometer. Via an II X-ray photoelectron spectrometer by operating Al Kα radiation (1486.71 eV), X-ray photoelectron spectroscopy (XPS) was obtained. The surface area properties of the catalyst were tested by collected by N₂ adsorption isotherm where Micromeritics TriStar II, 3020 was applied.

2.3. Electrochemical measurements

As a working electrode, glassy carbon (GC) with a cross-section area of 0.196 cm² was utilized by coating the polished mirror surface through the catalyst ink. The ink of the catalyst was prepared by sonicating 5.0 mg inside 980 μL of de-ionized/ethanol (v/v ≈ 1:9)/20 μL Nafion (5 wt%) mixture. As received, Pt supported on carbon (20 wt% Pt/C) was utilized as reference catalysts. As a reference electrode, an Hg/HgO was employed, nevertheless the acquired potentials then transformed to the reversible hydrogen electrode (RHE) measurement, $V_{RHE} = V_{Hg/HgO} + 0.059 \text{ pH} + V^{\theta}_{Hg/HgO}$. On the way to determine the number of transferred electrons, the K–L equations were used. In an electrolyte of 0.1 M KOH, at ambient temperature via a workstation (CHI 660E), the entire electrochemical performances were checked. At a scan rate of 5 mV s⁻¹, by the means of the rotary disk electrode system, the linear sweep voltammetry (LSV) was achieved. Using a scan rate of 10 mV s⁻¹, through static-electrode condition, the cyclic voltammogram (CV) was then carried out. The resistance to intermediate molecules released from fuel oxidation in addition to ORR time-dependent stability were indicated using chronoamperometry. Electrochemically, the prepared electrode was cleansed and reached to the steady-state in a fresh electrolyte at 0.1 V s⁻¹ before tests.

2.4. Fabrication of home-made zinc-air batteries

2.4.1. Primary zinc-air battery

Through a liquid homemade assembled battery, a primary zinc-air battery was used. As shown in Fig. S8a, the cathode was made from a carbon sheet of 1 cm × 1 cm size and 1.0 mg cm⁻² loaded catalyst, meanwhile, a zinc foil was used as the anode. An

electrolyte of zinc acetate and potassium hydroxide of 0.2 M and 6.0 M, respectively, was used.

2.4.2. All-solid-state zinc-air battery

As an anode, a zinc sheet (~99,98% metal base) and a solid polymeric electrolyte as a separator were used. Polyvinyl alcohol powder (4.5 g) was left to disperse at 90 °C in 45 mL of KOH/ZnAc (0.1:0.02 M) to form a uniform gelatinous solution to form the solid polymer electrolyte, accompanied by pouring the thin polymer film on a glass disk (Fig. S8b). The film was frozen and thawed 12 h before being used. A thin layer from the catalyst ink was cast over one face of the solid electrolyte and over the other opposite face the zinc piece was fixed, followed by adding nickel mesh as a current collector on the layer of the ambient catalyst, then the battery was assembled. The constituent elements were compressed tightly through roll-pressing accompanied by annealing at 65 °C to eliminate solvents before electrochemical processing. The load of the catalyst remained 5.0 mg cm^{-2}. There was no need for an inert atmosphere or glove box for packaging.

3. Results and discussion

3.1. Synthetic process, morphology and structure analysis

The preparation process for Fe$_3$N encapsulated in ZIF-8 (ZFN) is depicted in Fig. 1a. Briefly, Fe$_2$O$_3$ nanoparticles are obtained hydrothermally, then converted to Fe$_3$N. Fe$_3$N nanoparticles are later dispersed in methanol solution followed by the evolution of Fe$_3$N encapsulated in ZIF-8 (ZFN) frameworks.

From the TEM image and corresponding elemental mapping (Fig. 1b–e), it demonstrates that N and C are allocated uniformly all over the entire architecture, whereas Fe and partial-N were largely distributed in the form of dispersed nanoparticles. The HRTEM image (Fig. 1f) further verifies that Fe$_3$N nanoparticles are encapsulated in ZFN-900, including lattice spaces and planes of d$_{(110)}$ = 0.2 nm, d$_{(100)}$ = 0.43 nm (Fig. 1g). As shown in the inset of Fig. 1g, the selected-area electron diffraction (SAED) image for ZFN-900 reveals the diffraction rings of (100), and (110) facets of Fe$_3$N, affirming the polycrystalline nature of Fe$_3$N, consistent with XRD and HRTEM results.

Raman spectrum (Fig. 1h) of ZFN-900 reveals the G-peak at 1591 cm^{-1} and the D-peak at 1330 cm^{-1}. The G-peak is caused by the bond stretching of entire sp^2-bonded pairs (C=C/N=C), whereas the D-peak is attributed to the sp^3 defect sites. Moreover, the I_D/I_G ratio of ZFN-900 is about 1.11, demonstrating the low graphitization degree with abundant defective sites in ZFN-900 [26]. An expanded 2D-band can be seen at about 2771 cm^{-1}, indicating the growth of graphitic films in the porous carbon materials [27,28].

X-ray diffraction (XRD) patterns of Fe$_2$O$_3$, Fe$_3$N, ZFN and ZFN-900 are exposed in Fig. 2a. The ZFN-XRD pattern agrees with that of ZIF-8 nanocrystals. After carbonization (ZFN-900), ZIF-8 nanocrystals are entirely transformed into N/C [24]. Herein, the high diffraction peak at 2θ = 23.9° and 43.9° is assigned to (002) and (101) planes of carbon, respectively [19,29]. Besides, there is a small peak at about 43° in the ZFN-900 sample, evidencing the presence of Fe$_3$N.

Brunauer-Emmett-Teller (BET) analysis was achieved in pursuance of detecting the specific surface areas of catalysts through their nitrogen adsorption-desorption isotherms. ZFN, ZFN-900, Fe$_2$O$_3$, Fe$_3$N isotherms are presented in Fig. 2b and Fig. S2. The surface area and pore width of ZFN are 1531 m^2 g^{-1} and 1.88 nm, respectively, whereas those of ZFN-900 correspond to 1027 m^2 g^{-1} and 2.3 nm. Also, the measured BET surface area for Fe$_2$O$_3$ is 25 m^2 g^{-1}, whereas 17 m^2 g^{-1} for Fe$_3$N, considerably not more that

of ZFN-900. The contraction of the surface area of ZFN-900 correlated with the as-prepared-ZFN is mainly accredited to wrinkling of the N doped carbon fragments thanks to inequality in bond length of iron/nitrogen, carbon/nitrogen and carbon/carbon bonds [24,30].

Morphologies of Fe$_3$N, ZFN and ZFN-900 were observed through SEM besides TEM images. As presented in Fig. 2c–e, Fe$_3$N shows the nanoparticle state with average width ≈74.6 nm (Fig. 2c). Also, Fig. S3 displays the existence of Fe$_2$O$_3$ nanoparticles with a nano-sized domain of around 70 nm. ZFN has a morphology of rhombic dodecahedron (Fig. 2d), indicating that the polyhedron form of the as-prepared ZFN nanocrystals is well-maintained fixed shape even after embedding Fe$_3$N inside it.

By the analysis of XPS, as exhibited in Fig. 2f–h and Fig. S1, it displays the existence of C, N, Fe and Zn elements in samples. After pyrolysis at 900 °C, the N, C, Fe, Zn content (Fig. S1c) of the obtained Fe$_3$N embedded carbon doped with nitrogen (ZFN-900) is 3.84%, 95.53%, 0.33% and 0.3%, respectively. The N 1s peak (Fig. 2g and S1d) is deconvoluted into three peaks of pyridinic-N (25%), graphitic-N (64%) and pyrrolic-N (11%). The pyridinic-N could improve the surface wettability besides onset potential [24,31,32], while graphitic-N could boost the diffusion-limiting properties [24,33]. The peak of C 1s (Fig. 2h) similarly is deconvoluted into two peaks for C–C with C=C (51.5%), and C–N (48.5%). Moreover, Fe 2p displays major peaks of Fe 2p$_{3/2}$ (711 eV) and Fe 2p$_{1/2}$ (723 eV) (Fig. S1a), while Zn exhibits major peaks of Zn 2p$_{3/2}$ (1022 eV) and Zn 2p$_{1/2}$ (1045 eV) (Fig. S1b). In view of the aforementioned XPS for ZFN-900, the obtained data indicate the formation of N-doped carbon with very small traces of zinc (~0.36%) which have no influence on the catalytic activity [24].

3.2. Electrocatalytic performance

From the cyclic voltammetry (Fig. 3a), it indicates that ZFN-900 has an obvious activity in an O$_2$-saturated electrolyte. Besides, as it can be seen from Fig. 3a, there is a cathodic current peak emerging at ≈0.80 V, compared to that within a N$_2$-saturated solution, demonstrating a promising ORR electrocatalytic performance. To evaluate the synergistic effects of the chemical composition on the electrocatalytic efficiency, linear sweep voltammetry (Fig. 3b) was employed. In 0.1 M KOH solution, the exceptional ORR performance for ZFN-900 was investigated, exhibiting a larger half-wave potential ($E_{1/2}$) of 0.85 V than that of Pt/C (0.82 V) and N-doped carbon (0.71 V).

To acquire further insight into the reaction mechanism, the Tafel slopes were detected. As can be seen in Fig. 3c, Tafel slope for ZFN-900 is 53 mV dec^{-1}, lower than that for Pt/C (78 mV dec^{-1}), N-doped carbon (90 mV dec^{-1}) and Fe$_3$N (99 mV dec^{-1}), indicating faster reaction kinetics in ZFN-900. Furthermore, the outstanding ORR efficiency and Tafel slopes for ZFN-900 were also compared with other analogous non-noble materials, and it is obviously the one of the most efficient ORR electrocatalysts (Table S2). Similarly, for ZFN-900, its kinetic current density obtained by means of the Koutecky-Levich (K-L) approach displays a proportional increase with the raised rate of rotation. As presented in the inset in Fig. 3d, the n value was calculated to be ≈ 4.0 in a potential window of 0.3–0.7 V, suggesting first-order reaction kinetics, four-electron pathway of ORR for ZFN-900, the same to the theoretical value of Pt/C (4.0) [24]. Likewise, ZFN-900 shows excellent ORR stability (Fig. S5b), as revealed by no obvious shifts of LSV curves after 2000 cycles. The high stability was further verified by utilizing the chronoamperometric (i–t) obtained plot. Fig. 3e displays that ZFN-900 keeps a comparatively small current reduction, which has only 9% drop later after a long-time chronoamperometric test, whereas Pt/C reveals a 27% reduction in current densities. The small current reduction (i–t) for ZFN-900 could be attributed to the exceptional
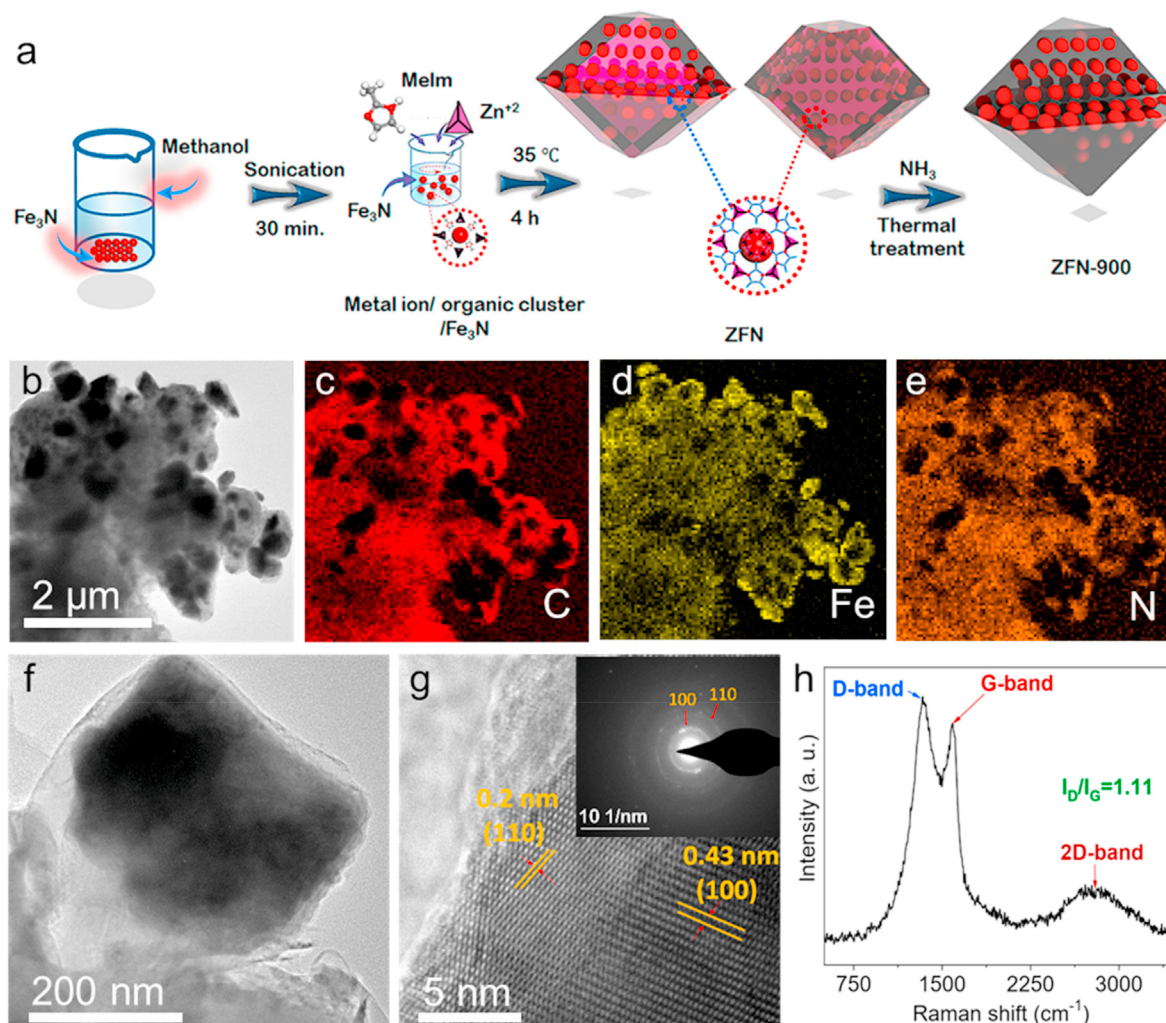
Fig. 1. (a) Synthesis route for ZFN in 3d structure; (b) TEM image of ZFN-900; (c-e) and EDX mapping of elemental distribution of ZFN-900; (f, g) HRTEM images of Fe_3N inside ZFN-900 and the inset of (g) is the SAED pattern of Fe_3N; (h) Raman spectra of ZFN-900. (A colour version of this figure can be viewed online.)

encapsulation structure impedes the collapse of the Fe_3N nanoparticles, and the protective effect of the carbon layers surrounding Fe_3N nanoparticles can minimize agglomeration of metal nitride nanoparticles, which is advantageous for the durability of ZFN-900 catalysts compared with that of Pt/C. As can be seen in Fig. S6, the iron nitride nanoparticles are still completely well capsulated after 2000 cycles. Furthermore, methanol tolerance was evaluated throughout chronoamperometric (i−t), by adding 1 M methanol. As exhibited in Fig. 3f, the current density of carbon-supported Pt drops severely, while for ZFN-900 it recovers quickly next to a temporary disorder, indicating the superb methanol resistance ability.

To examine the correlation between the electrocatalytic activity and the calcination temperature, the as-synthesized samples were annealed at 800, 900 and 1000 °C. As can be seen, Fig. S7 displays the obtained curves from LSV indicating that ZFN-800 and ZFN-1000 have poor catalytic activity relative to ZFN-900. Consistent with the fitted results for N 1s of ZFN-800, the pyrrolic-N, pyridinic-N and graphitic-N are 27%, 55% and 18%, respectively, while ZFN-1000 contain overwhelming graphitic-N (74%) (see Fig. S1). The low ORR activity of ZFN-800 is maybe owing to a particular amount of inadequate pyridinic-N. ZFN-1000 still remains a high limiting current density as a consequence of the plentiful graphitic-N

nevertheless the onset potential is inefficient due to the deficient of pyridinic-N. Hereafter, the optimum calcination temperature is 900 °C. In such a case, appropriate amounts of pyridinic-N with graphitic-N, and Fe_3N could lead to the highest ORR activity for ZFN-900. Furthermore, ZFN-900 electrochemical double-layer capacitance (Cdl) which is directly proportional to the electrochemical active surface area (ECSA) was indicated. As shown and explained in details in the supporting information (Fig. S8), ZFN-900 shows a large surface area with exposed active sites. The results of the characterization and evaluation of ORR activity can provide a clear insight into the active sites in ZFN-900 where Fe_3N species and N-doped carbon act as active site to catalyze the ORR at the interface of iron nitrides and carbon support [34]. The uniformly dispersed Fe_3N nanoparticles with small size afford plenty of efficient Fe−N−C catalytic active sites. Hence, in this work, Fe−N−C is regarded as the active site in the ORR.

The electrochemical impedance spectroscopy (EIS) measurement for the catalysts was measured. Fig. S5 exhibits Nyquist plots of ZFN-900, C/N, Fe_3N and carbon-supported Pt in high-frequency area with high-frequency intercepts identical to the electrolyte resistance. In addition, the low-frequency intercepts are equivalent to the summation of electrolyte resistance along with charge transfer resistance [4,5]. The electron transfer resistance of ZFN-
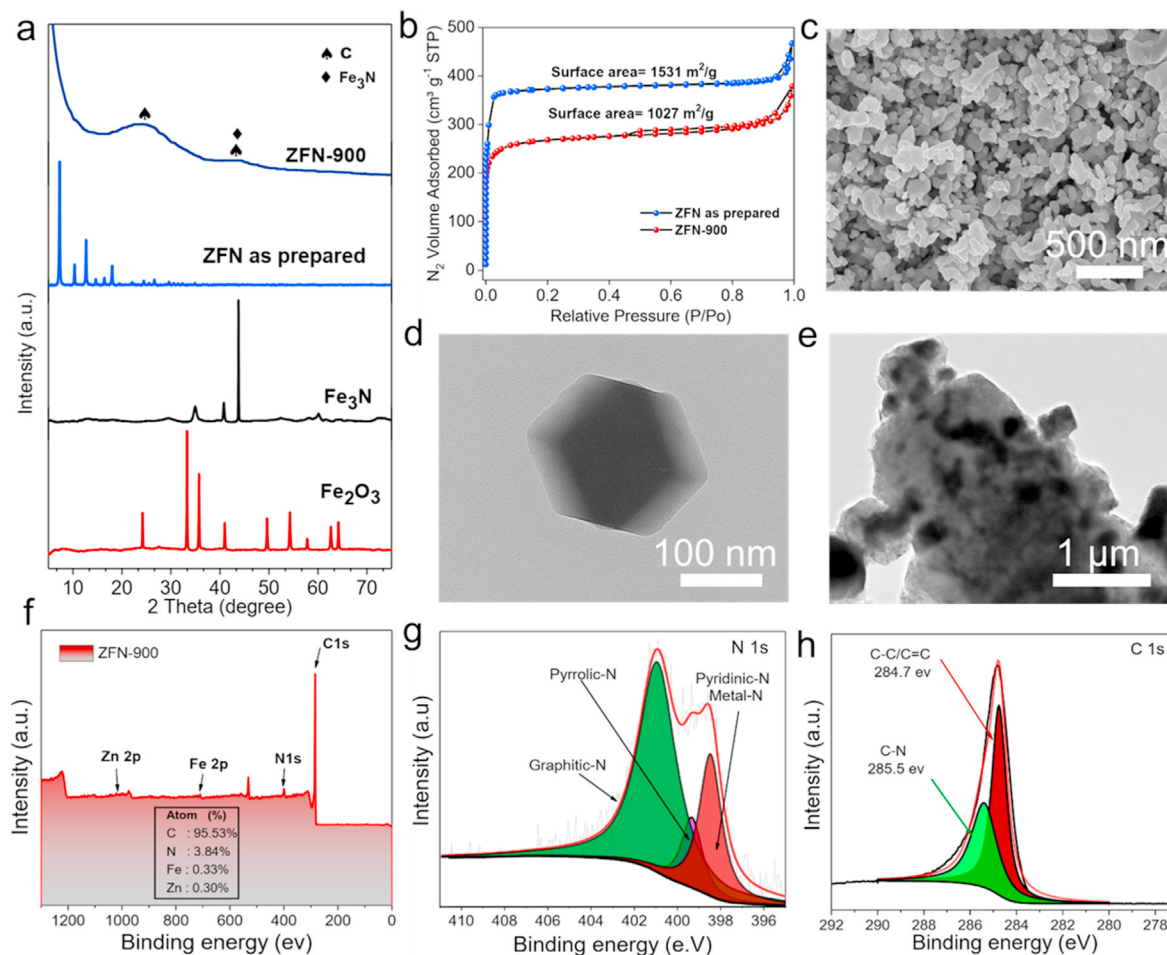
Fig. 2. (a) XRD patterns of Fe_2O_3, Fe_3N, as-prepared ZFN and ZFN-900; (b) Nitrogen desorption-desorption isotherms of the as-formed ZFN and ZFN-900; (c) FESEM image of Fe_3N nanoparticles; (d, e) TEM images for ZFN and ZFN-900, respectively; (f) XPS spectra survey scan; (g) N 1s spectra; (h) C 1s spectra of ZFN-900. (A colour version of this figure can be viewed online.)

900 is only 4.8 Ω, lower than that of carbon-supported Pt (24.5 Ω), demonstrating the well-maintained high conductivity for ZFN-900 (Table S1). It may be stated that low charge transfer resistance demonstrates a robust combination among Fe_3N and N/C, which can extensively modify the electronic structure of ZFN-900, therefore improving the ORR catalytic activity.

3.3. Performance of primary and all-solid-state Zn−Air batteries

By reason of high ORR activity [2,35], Fe-based materials are considered as high-efficiency candidates with regard to primary Zn-air batteries (ZABs) [36−42]. Fig. 4a presents a peak of the power density for ZFN-900 at ≈ 115.8 mW cm^{-2} at a current density of 190.7 mA cm^{-2}, much higher than that of Pt/C (81.6 mW cm^{-2}) at 130.8 mA cm^{-2}. Primary and traditional solid zinc-air batteries with two electrodes were made-up as explained in Fig. 4d and Fig. S9. As shown in Fig. 4c, an open circuit voltage of 1.42 V for the as-formed ZFN-900 primary battery is revealed, confirming the feasibility of ZFN-900 employed in Zn-air batteries (Fig. 4b).

With regard to determining the applicability and prospects of ZFN-900 electrodes, an All-Solid-State (ASS) ZABs was assembled in accordance with Fig. S9b. Impressively, an open-circuit voltage of 1.21 V (Fig. 4e) is present from the ASS battery. Furthermore, the three assembled batteries are successfully able to power a LED with

high voltage (Fig. 4f). This indicates that ZFN-900 ASS ZAB represents an extraordinary promise for high power ZABs applications. It is worthy to conclude that the exceptional power density along with current density for ZFN-900 cathode relative to the other non-noble materials in Zn-air batteries (Table S2), could be attributable to the large surface area, structural synergistic effect and the presence of the Fe_3N encapsulated in the nitrogen-rich carbon frameworks. It is also worth pointing out that the overall activity of FeN_x toward ORR, OER, HER and Zn−air batteries is significantly superior to the very recently reported as a trifunctional electrocatalyst including FeN_x/carbon [43], Fe_2N/Fe_3N [44] and H−Co@FeCo/N/C [45].

4. Conclusions

Briefly, the Fe_3N nanoparticles embedded in N-doped carbon frameworks acquired from ZIFs were easily prepared as an extremely active ORR electrocatalyst. Attributed to Fe−N−C active site, high N doping content, mesoporous framework with exceptional specific surface area (1027 m^2 g^{-1}), a superior rational-designed and highly active catalyst for ORR was obtained, with a half-wave potential of 0.85 V, high stability, and methanol resistance capability in contrast with commercial Pt/C catalysts in 0.1 M KOH. Exceptionally, the ZFN-900 air-cathode exhibited a raised
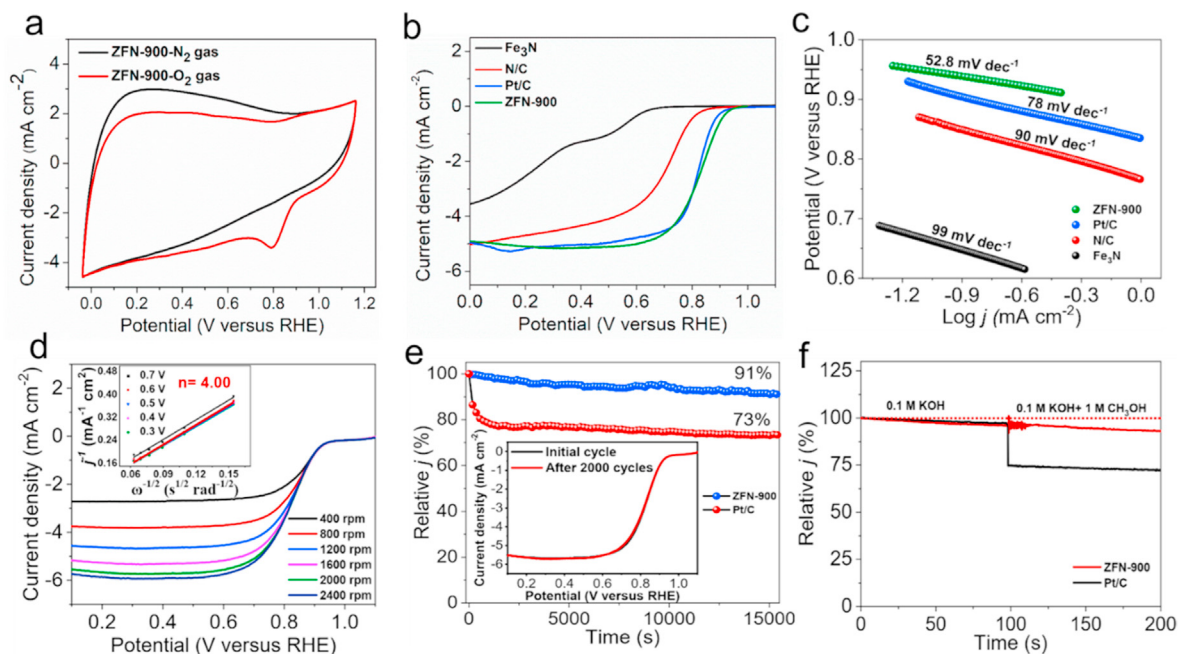
Fig. 3. (a) CV curves of ZFN-900 in N_2- and O_2-saturated 0.1 M KOH solution with a scan rate of 100 mV s^{-1}; (b) ORR polarization curves of different catalysts at 1600 rpm; (c) Tafel slopes of different catalysts derived from ORR LSV curves; (d) LSVs for ZFN-900 at various rotating speeds, inset is the corresponding *K−L* plot; (e) Time dependent chronoamperometric (*i* versus *t*) profiles of ZFN-900 and Pt/C at 0.6 V, the inset in (e) shown LSV of ZFN-900 before and after 2000 cv cycles; (f) Time dependent chronoamperometric (*i* versus *t*) profile of ZFN-900 and Pt/C before and after 1.0 M methanolic solution injection. (A colour version of this figure can be viewed online.)
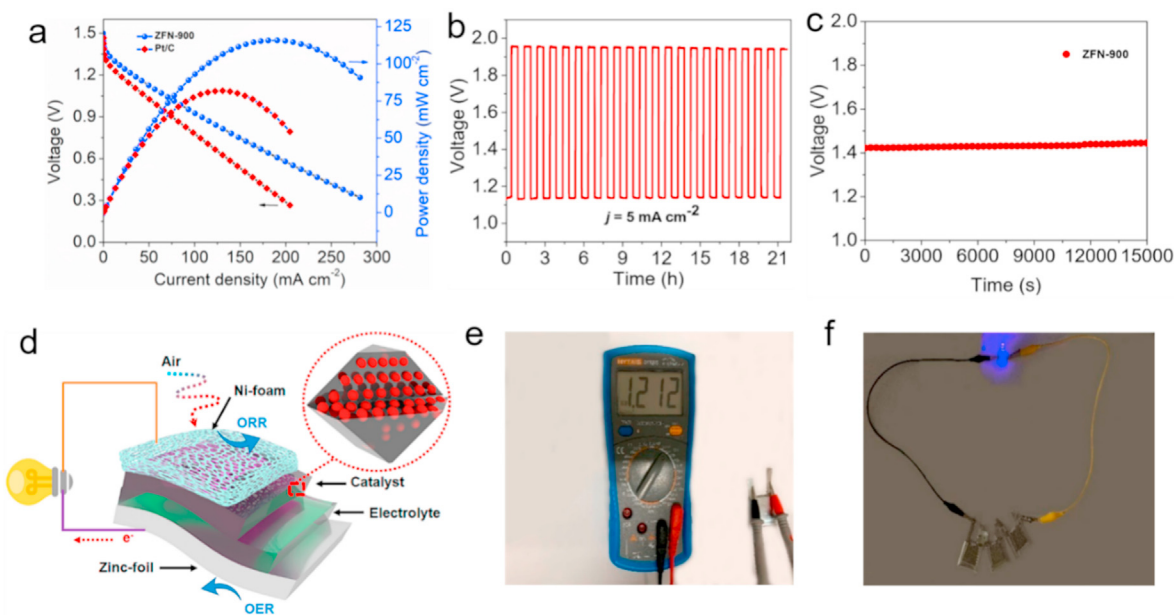

Fig. 4. Fabrication and performance of ZFN-900 based zinc−air batteries. (a) *V-j* polarization and corresponding power density profiles; (b) Galvanostatic discharge−charge cycling profiles of ZFN-900 at high current density with a cycling interval of 1 h; (c) Open circuit potential for the ZFN-900 based primary Zn-air battery; (d) Schematics of home-made all-solid-state zinc-air battery; (e) Photograph of the assembled all-solid-state zinc-air battery exhibiting a minimum open-circuit voltage of ≈1.212 V; (f) Photograph of a lighted light emitting diode (LED) powered by the all-solid-state Zn-air batteries. (A colour version of this figure can be viewed online.)

peak power density of 115.9 mW cm^{-2} along with exceptional durability. This research reveals a novel potential for a rational design for energy conversion applications of high-performance economical-metal catalysts.

Declaration of AFMRC project

This paper is not based on AFMRC Project.

Author declaration

We wish to confirm that there are no known conflicts of interest associated with this publication and there has been no significant financial support for this work that could have influenced its outcome.

We confirm that the manuscript has been read and approved by all named authors and that there are no other persons who satisfied

the criteria for authorship but are not listed. We further confirm that the order of authors listed in the manuscript has been approved by all of us.

We confirm that we have given due consideration to the protection of intellectual property associated with this work and that there are no impediments to publication, including the timing of publication, with respect to intellectual property. In so doing we confirm that we have followed the regulations of our institutions concerning intellectual property.

We understand that the Corresponding Author is the sole contact for the Editorial process (including Editorial Manager and direct communications with the office). He/she is responsible for communicating with the other authors about progress, submissions of revisions and final approval of proofs. We confirm that we have provided a current, correct email address which is accessible by the Corresponding Author and which has been configured to accept email from msc@whut.edu.cn.

CRediT authorship contribution statement

Amr Radwan: Methodology, Writing - original draft, preparation. **Huihui Jin:** Software. **Bingshuai Liu:** Data curation. **Zibo Chen:** Visualization. **Qian Wu:** Investigation. **Xin Zhao:** Software. **Daping He:** Conceptualization, Writing - review & editing, Reviewing and Editing, Validation. **Shichun Mu:** Conceptualization, Writing - review & editing, Reviewing and Editing, Validation.

Declaration of competing interest

The authors declare that they have no known competing financial interests or personal relationships that could have appeared to influence the work reported in this paper.

Acknowledgements

Appendix A. Supplementary data

Supplementary data to this article can be found online at https://doi.org/10.1016/j.carbon.2020.09.024.

References

[1] Z. Wang, H. Jin, T. Meng, K. Liao, W. Meng, J. Yang, D. He, Y. Xiong, S. Mu, Fe, Cu-coordinated ZIF-derived carbon framework for efficient oxygen reduction reaction and zinc—air batteries, Adv. Funct. Mater. 28 (39) (2018) 1802596.
[2] M. Wang, Y. Yang, X. Liu, Z. Pu, Z. Kou, P. Zhu, S. Mu, The role of iron nitrides in the Fe—N—C catalysis system towards the oxygen reduction reaction, Nanoscale 9 (22) (2017) 7641—7649.
[3] J. Zhu, W. Li, S. Li, J. Zhang, H. Zhou, C. Zhang, J. Zhang, S. Mu, Defective N/S-Co doped 3D cheese-like porous carbon nanomaterial toward efficient oxygen reduction and Zn—air batteries, Small 14 (21) (2018) 1800563.
[4] A. Radwan, Y. Liu, Y. Qi, W. Jin, V. Nguyen, X. Yang, S. Yang, W. Chen, Cycling stability of carbon coated Na$_5$V$_{12}$O$_{32}$ ultralong nanowires as a cathode material for sodium-ion batteries, Mater. Res. Bull. 97 (2018) 24—29.
[5] A.R. Radwan, Y. Liu, V. Nguyen, W. Chen, Sodium vanadate nanoflowers/rGO composite as a high-rate cathode material for sodium-ion batteries, J. Mater. Sci. Mater. Electron. 29 (8) (2018) 7032—7039.
[6] M. Wang, C. Zhang, T. Meng, Z. Pu, H. Jin, D. He, J. Zhang, S. Mu, Iron oxide and phosphide encapsulated within N, P-doped microporous carbon nanofibers as advanced tri-functional electrocatalyst toward oxygen reduction/evolution and hydrogen evolution reactions and zinc—air batteries, J. Power Sources 413 (2019) 367—375.
[7] M. Zhang, Q. Dai, H. Zheng, M. Chen, L. Dai, Novel MOF-derived Co@N-C bifunctional catalysts for highly efficient Zn—air batteries and water splitting, Adv. Mater. 30 (10) (2018) 1705431.
[8] H. Osgood, S.V. Devaguptapu, H. Xu, J. Cho, G. Wu, Transition metal (Fe, Co, Ni, and Mn) oxides for oxygen reduction and evolution bifunctional catalysts in alkaline media, Nano Today 11 (5) (2016) 601—625.
[9] L. Chai, L. Zhang, X. Wang, Z. Hu, Y. Xu, T.-T. Li, Y. Hu, J. Qian, S. Huang, Cube-shaped metal-nitrogen—carbon derived from metal-ammonia complex-impregnated metal-organic framework for highly efficient oxygen reduction reaction, Carbon 158 (2020) 719—727.
[10] Y. Zhang, N. Wang, N. Jia, J. Wang, J. Sun, F. Shi, Z.-H. Liu, R. Jiang, A low-cost and facile method for the preparation of Fe-N/C-based hybrids with superior catalytic performance toward oxygen reduction reaction, ccAdv. Mater. Interf. 6 (8) (2019) 1900273.
[11] H. Wang, F. Yin, B. Chen, G. Li, Synthesis of an ε-MnO$_2$/metal—organic-framework composite and its electrocatalysis towards oxygen reduction reaction in an alkaline electrolyte, J. Mater. Chem. 3 (31) (2015) 16168—16176.
[12] C. Zhu, Z. Yin, W. Lai, Y. Sun, L. Liu, X. Zhang, Y. Chen, S.-L. Chou, Fe-Ni-Mo nitride porous nanotubes for full water splitting and Zn-Air batteries, Adv. Energy Mater. 8 (36) (2018) 1802327.
[13] W.Y. Noh, J.H. Lee, J.S. Lee, Nitrogen-doped carbon nanotube—graphene hybrid stabilizes M$_x$N (M = Fe, Co) nanoparticles for efficient oxygen reduction reaction, Appl. Catal., B 268 (2020) 118415.
[14] T. Li, M. Li, M. Zhang, X. Li, K. Liu, M. Zhang, X. Liu, D. Sun, L. Xu, Y. Zhang, Y. Tang, Immobilization of Fe$_3$N nanoparticles within N-doped carbon nanosheet frameworks as a high-efficiency electrocatalyst for oxygen reduction reaction in Zn-air batteries, Carbon 153 (2019) 364—371.
[15] Y. Zheng, F. He, J. Wu, D. Ma, H. Fan, S. Zhu, X. Li, Y. Lu, Q. Liu, X. Hu, Nitrogen-doped carbon nanotube—graphene frameworks with encapsulated Fe/Fe$_3$N nanoparticles as catalysts for oxygen reduction, ACS Appl. Nano Mater. 2 (6) (2019) 3538—3547.
[16] Y. Deng, B. Chi, J. Li, G. Wang, L. Zheng, X. Shi, Z. Cui, L. Du, S. Liao, K. Zang, J. Luo, Y. Hu, X. Sun, Atomic Fe-doped MOF-derived carbon polyhedrons with high active-center density and ultra-high performance toward PEM fuel cells, Adv. Energy Mater. 9 (13) (2019) 1802856.
[17] Y.-R. Lee, M.-S. Jang, H.-Y. Cho, H.-J. Kwon, S. Kim, W.-S. Ahn, ZIF-8: a comparison of synthesis methods, Chem. Eng. J. 271 (2015) 276—280.
[18] G. Zhong, D. Liu, J. Zhang, The application of ZIF-67 and its derivatives: adsorption, separation, electrochemistry and catalysts, J. Mater. Chem. 6 (5) (2018) 1887—1899.
[19] J. Tang, R.R. Salunkhe, J. Liu, N.L. Torad, M. Imura, S. Furukawa, Y. Yamauchi, Thermal conversion of core—shell metal—organic frameworks: a new method for selectively functionalized nanoporous hybrid carbon, J. Am. Chem. Soc. 137 (4) (2015) 1572—1580.
[20] C. Wan, X. Duan, Y. Huang, Molecular design of single-atom catalysts for oxygen reduction reaction, Adv. Energy Mater. 10 (14) (2020) 1903815.
[21] L. Zhu, D. Zheng, Z. Wang, X. Zheng, P. Fang, J. Zhu, M. Yu, Y. Tong, X. Lu, A confinement strategy for stabilizing ZIF-derived bifunctional catalysts as a benchmark cathode of flexible all-solid-state zinc—air batteries, Adv. Mater. 30 (45) (2018) 1805268.
[22] Q. Cheng, C. Yang, K. Tao, L. Han, Inlaying ZIF-derived Co$_3$S$_4$ hollow nanocages on intertwined polypyrrole tubes conductive networks for high-performance supercapacitors, Electrochim. Acta 341 (2020) 16042.
[23] C. Lu, X. Chen, Sea-island nanostructured polyvinylidene fluoride/zeolitic imidazolate framework-8 polyelectrolyte for high-performance all-solid-state supercapacitors, J. Power Sources 448 (2020) 227587.
[24] I.S. Amiinu, X. Liu, Z. Pu, W. Li, Q. Li, J. Zhang, H. Tang, H. Zhang, S. Mu, From 3D ZIF nanocrystals to Co—N$_x$/C nanorod array electrocatalysts for ORR, OER, and Zn—air batteries, Adv. Funct. Mater. 28 (5) (2018) 1704638.
[25] I.S. Amiinu, Z. Pu, X. Liu, K.A. Owusu, H.G.R. Monestel, F.O. Boakye, H. Zhang, S. Mu, Multifunctional Mo—N/C@MoS$_2$ electrocatalysts for HER, OER, ORR, and Zn—Air batteries, Adv. Funct. Mater. 27 (44) (2017) 1702300.
[26] J. Zhang, Y. Sun, J. Zhu, Z. Kou, P. Hu, L. Liu, S. Li, S. Mu, Y. Huang, Defect and pyridinic nitrogen engineering of carbon-based metal-free nanomaterial toward oxygen reduction, Nanomater. Energy 52 (2018) 307—314.
[27] E. Dervishi, Z. Ji, H. Htoon, M. Sykora, S.K. Doorn, Raman spectroscopy of bottom-up synthesized graphene quantum dots: size and structure dependence, Nanoscale 11 (35) (2019) 16571—16581.
[28] A. Virga, C. Ferrante, G. Batignani, D. De Fazio, A. Nunn, A. Ferrari, G. Cerullo, T. Scopigno, Coherent anti-Stokes Raman Spectroscopy of single and multi-layer graphene, Nat. Commun. 10 (1) (2019) 1—9.
[29] J. Li, S. Ghoshal, W. Liang, M.-T. Sougrati, F. Jaouen, B. Halevi, S. McKinney, G. McCool, C. Ma, X. Yuan, Structural and mechanistic basis for the high activity of Fe—N—C catalysts toward oxygen reduction, Energy Environ. Sci. 9 (7) (2016) 2418—2432.
[30] I.S. Amiinu, J. Zhang, Z. Kou, X. Liu, O.K. Asare, H. Zhou, K. Cheng, H. Zhang, L. Mai, M. Pan, Self-organized 3D porous graphene dual-doped with biomass-sponsored nitrogen and sulfur for oxygen reduction and evolution, ACS Appl. Mater. Interfaces 8 (43) (2016) 29408—29418.
[31] K. Sakaushi, T.P. Fellinger, M. Antonietti, Bifunctional metal-free catalysis of mesoporous noble carbons for oxygen reduction and evolution reactions, ChemSusChem 8 (7) (2015) 1156—1160.
[32] K. Sakaushi, K. Uosaki, Highly efficient oxygen and hydrogen electrocatalytic activities of self-morphogenic nanoporous carbon, Nitrogen Architectures, ChemNanoMat 2 (2) (2016) 99—103.
[33] L.-M. Zhang, Z.-B. Wang, J.-J. Zhang, X.-L. Sui, L. Zhao, D.-M. Gu, Honeycomb-

like mesoporous nitrogen-doped carbon supported Pt catalyst for methanol electrooxidation, Carbon 93 (2015) 1050—1058.

[34] H. Yin, C. Zhang, F. Liu, Y. Hou, Hybrid of iron nitride and nitrogen-doped graphene aerogel as synergistic catalyst for oxygen reduction reaction, Adv. Funct. Mater. 24 (20) (2014) 2930—2937.

[35] J. Masud, S. Umapathi, N. Ashokaan, M. Nath, Iron phosphide nanoparticles as an efficient electrocatalyst for the OER in alkaline solution, J. Mater. Chem. 4 (25) (2016) 9750—9754.

[36] C.Y. Su, H. Cheng, W. Li, Z.Q. Liu, N. Li, Z. Hou, F.Q. Bai, H.X. Zhang, T.Y. Ma, Atomic modulation of FeCo—nitrogen—carbon bifunctional oxygen electrodes for rechargeable and flexible all-solid-state zinc—air battery, Adv. Energy Mater. 7 (13) (2017) 1602420.

[37] G. Fu, Z. Cui, Y. Chen, L. Xu, Y. Tang, J.B. Goodenough, Hierarchically mesoporous nickel-iron nitride as a cost-efficient and highly durable electrocatalyst for Zn-air battery, Nanomater. Energy 39 (2017) 77—85.

[38] J.-J. Cai, Q.-Y. Zhou, B. Liu, X.-F. Gong, Y.-L. Zhang, K. Goh, D.-M. Gu, L. Zhao, X.-L. Sui, Z.-B. Wang, A sponge-templated sandwich-like cobalt-embedded nitrogen-doped carbon polyhedron/graphene composite as a highly efficient catalyst for Zn—air batteries, Nanoscale 12 (2) (2020) 973—982.

[39] R. Ma, G. Lin, Q. Ju, W. Tang, G. Chen, Z. Chen, Q. Liu, M. Yang, Y. Lu, J. Wang, Edge-sited Fe-N4 atomic species improve oxygen reduction activity via boosting O_2 dissociation, Appl. Catal., B 265 (2020) 118593.

[40] Q. Zhou, Z. Zhang, J. Cai, B. Liu, Y. Zhang, X. Gong, X. Sui, A. Yu, L. Zhao, Z. Wang, Z. Chen, Template-guided synthesis of Co nanoparticles embedded in hollow nitrogen doped carbon tubes as a highly efficient catalyst for rechargeable Zn-air batteries, Nanomater. Energy 71 (2020) 104592.

[41] X. Zhang, X. Han, Z. Jiang, J. Xu, L. Chen, Y. Xue, A. Nie, Z. Xie, Q. Kuang, L. Zheng, Atomically dispersed hierarchically ordered porous Fe—N—C electrocatalyst for high performance electrocatalytic oxygen reduction in Zn-Air battery, Nanomater. Energy 71 (2020) 104547.

[42] Z. Zhang, H. Jin, J. Zhu, W. Li, C. Zhang, J. Zhao, F. Luo, Z. Sun, S. Mu, 3D flower-like ZnFe-ZIF derived hierarchical Fe, N-Co doped carbon architecture for enhanced oxygen reduction in both alkaline and acidic media, and zinc-air battery performance, Carbon 161 (2020) 502—509.

[43] J. Ding, P. Wang, S. Ji, H. Wang, V. Linkov, R. Wang, N-doped mesoporous FeN_x/carbon as ORR and OER bifunctional electrocatalyst for rechargeable zinc-air batteries, Electrochim. Acta 296 (2019) 653—661.

[44] Y. Hu, D. Huang, J. Zhang, Y. Huang, M.-S.J.T. Balogun, Y. Tong, Dual doping induced interfacial engineering of Fe_2N/Fe_3N hybrids with favorable d-band towards efficient overall water splitting, ChemCatChem 11 (24) (2019) 6051—6060.

[45] Y.-j. Wu, X.-h. Wu, T.-x. Tu, P.-f. Zhang, J.-t. Li, Y. Zhou, L. Huang, S.-g. Sun, Controlled synthesis of FeN_x-CoN_x dual active sites interfaced with metallic Co nanoparticles as bifunctional oxygen electrocatalysts for rechargeable Zn-air batteries, Appl. Catal., B 278 (2020) 119259.